The Influence of Surface and Precipitation Characteristics on TRMM Microwave Imager Rainfall Retrieval Uncertainty

N. CARR,[*,+] P.-E. KIRSTETTER,[+,#] Y. HONG,[@] J. J. GOURLEY,[#] M. SCHWALLER,[&] W. PETERSEN,[**] NAI-YU WANG,[++] RALPH R. FERRARO,[##] AND XIANWU XUE[@]

[*] *School of Meteorology, University of Oklahoma, Norman, Oklahoma*
[+] *Advanced Radar Research Center, National Weather Center, Norman, Oklahoma*
[#] *NOAA/National Severe Storms Laboratory, Norman, Oklahoma*
[@] *School of Civil Engineering and Environmental Sciences, University of Oklahoma, Norman, Oklahoma*
[&] *NASA Goddard Space Flight Center, Greenbelt, Maryland*
[**] *NASA Wallops Flight Facility, Wallops Island, Virginia*
[++] *I.M. Systems Group, College Park, Maryland*
[##] *NOAA/NESDIS, College Park, Maryland*

(Manuscript received 9 October 2014, in final form 10 February 2015)

ABSTRACT

Characterization of the error associated with quantitative precipitation estimates (QPEs) from spaceborne passive microwave (PMW) sensors is important for a variety of applications ranging from flood forecasting to climate monitoring. This study evaluates the joint influence of precipitation and surface characteristics on the error structure of NASA's Tropical Rainfall Measurement Mission (TRMM) Microwave Imager (TMI) surface QPE product (2A12). TMI precipitation products are compared with high-resolution reference precipitation products obtained from the NOAA/NSSL ground radar–based Multi-Radar Multi-Sensor (MRMS) system. Surface characteristics were represented via a surface classification dataset derived from NASA's Moderate Resolution Imaging Spectroradiometer (MODIS). This study assesses the ability of 2A12 to detect, classify, and quantify precipitation at its native resolution for the 2011 warm season (March–September) over the southern continental United States. Decreased algorithm performance is apparent over dry and sparsely vegetated regions, a probable result of the surface radiation signal mimicking the scattering signature associated with frozen hydrometeors. Algorithm performance is also shown to be positively correlated with precipitation coverage over the sensor footprint. The algorithm also performs better in pure stratiform and convective precipitation events, compared to events containing a mixture of stratiform and convective precipitation within the footprint. This possibly results from the high spatial gradients of precipitation associated with these events and an underrepresentation of such cases in the retrieval database. The methodology and framework developed herein apply more generally to precipitation estimates from other passive microwave sensors on board low-Earth-orbiting satellites and specifically could be used to evaluate PMW sensors associated with the recently launched Global Precipitation Measurement (GPM) mission.

1. Introduction

Precipitation is an important component of the hydrologic cycle and also affects the global circulation via latent heating. Consequently, accurate estimates of precipitation at the global scale are vital for a variety of hydrometeorological applications (Stephens and Kummerow 2007). Spaceborne sensors are particularly suited for quantitative precipitation estimates (QPEs) because of their quasi-global coverage and consistency in data availability across geopolitical boundaries (Bakker 2009). However, satellite precipitation estimates suffer from numerous poorly characterized and quantified sources of error, currently limiting their optimal assimilation into hydrologic and atmospheric models (Weng et al. 2007; Bauer et al. 2002). This study attempts to better characterize the uncertainties present in precipitation estimates obtained from low-Earth-orbiting (LEO) passive microwave (PMW) sensors, with a specific emphasis on precipitation estimates from NASA's Tropical Rainfall Measurement Mission

Corresponding author address: Nick Carr, Advanced Radar Research Center, National Weather Center, 120 David L. Boren Blvd., Rm. 4630, Norman, OK 73072-7303.
E-mail: n.carr2@ou.edu

DOI: 10.1175/JHM-D-14-0194.1

(TRMM) Microwave Imager (TMI). Prior to the recent launch of the Global Precipitation Measurement (GPM) mission's core satellite and associated PMW sensor GMI, TMI acted as a benchmark for other PMW sensors, and consequently, its error characterization is particularly important from a satellite QPE standpoint (Hou et al. 2001). While there are numerous uncertainties associated with PMW precipitation retrievals [e.g., (mis)detection of precipitation, indirect information on the surface precipitation rate, and underconstrained nature of the precipitation retrieval; see Stephens and Kummerow (2007) for more information], this study focuses on two of the most significant: the underlying surface properties and the characteristics of the precipitation field within the sensor footprint.

Over the ocean, microwave emissivity is low and highly polarized, allowing PMW sensors to (largely) separate the surface radiation signal and the (warm) emission signal arising from liquid hydrometeors. However, over the land surface the microwave emissivity is higher and more variable because of its complex relationship with a number of highly variable (in space and time) surface characteristics such as soil moisture, roughness, vegetation properties, canopy, and snow cover (Aires et al. 2011). The high and variable surface emissivity largely obscures the lower-frequency emission signals, and overland PMW precipitation estimates instead rely primarily on brightness temperature Tb depressions resulting from microwave scattering by ice-phase hydrometeors. The variations in overland surface emissivity can be comparable in magnitude to the ice-scattering signal, and consequently, surface emissivity variations are a source of considerable uncertainty in PMW retrievals (Gopalan et al. 2010). Efforts are currently underway to better characterize land surface emissivity (Ferraro et al. 2013), and GPM-era PMW sensors will utilize a database of surface properties (such as emissivity) to constrain their overland retrievals and apply a Bayesian algorithm similar to that currently applied by the 2A12 ocean algorithm. However, at this time the effects of surface property variations on PMW retrievals are not well understood or quantified, and consequently, a major aim of this study is to determine what (if any) impacts the underlying surface characteristics have on the quality of PMW precipitation retrievals.

A second significant source of error/uncertainty in PMW precipitation estimates is the characteristics of the precipitation field within the sensor footprint (Varma et al. 2004). Specifically, the spatial distribution of precipitation within the footprint and the precipitation's microphysical characteristics can significantly impact the quality of PMW rainfall estimates. The relatively large footprint size of many PMW sensors (~7 km in the case of TMI's 85-GHz channel) often causes precipitation estimates of small-scale precipitation features to be degraded, particularly when high gradients of precipitation intensity are present within the footprint. The microphysical characteristics of precipitation (i.e., hydrometeor phase, size distribution, and shape) directly influence the radiances retrieved by PMW sensors and therefore must be taken into account during the retrieval process. Currently, the spatial and microphysical properties of precipitation are accounted for in bulk via a stratiform–convective classification scheme. However, because of the limited information available from PMW retrievals (particularly over the land), the outputs of this classification algorithm are inherently uncertain, and because of the link between the classification and precipitation estimation algorithms, misclassification can lead to significant errors in rainfall quantification.

This primary objective of this study is to assess the influence of surface and precipitation characteristics on the TMI QPE 2A12 product (version 7; Kummerow et al. 1998; McCollum and Ferraro 2003; Wang et al. 2009; Gopalan et al. 2010). Such an assessment is particularly valuable because of the recent launch of the GPM, which will utilize PMW precipitation estimates both from its core satellite (GMI) and its constellation sensors, in order to create a quasi-global precipitation observation network. The methodology presented herein could thus be readily adapted and utilized to evaluate PMW precipitation retrievals from other platforms.

This study builds on a framework that has previously been used to evaluate both the TRMM precipitation radar (PR) QPE and also QPE from PMW sensors (Kirstetter et al. 2012, 2014). Specifically, TMI's precipitation estimates are evaluated at pixel level relative to an external and independent reference precipitation estimate derived from NOAA/NSSL's ground radar–based National Mosaic and Multi-Sensor QPE (NMQ) Q2 system [note this system has since become the Multi-Radar Multi-Sensor (MRMS/Q3) system]. To minimize uncertainties caused by temporal resampling, the errors in the 2A12 estimates are characterized at the snapshot (rain rates) time scale (Wolff and Fisher 2009). Because of the many error sources that can affect ground radar QPE, it is impossible to "validate" the 2A12 estimates in a strict sense. However, the quality of the reference ground radar estimates is enhanced through a rigorous processing algorithm, making it a useful independent reference to help identify possible biases and general levels of uncertainty associated with the 2A12 precipitation estimates. To evaluate the influence of surface characteristics on the PMW retrievals, a surface type classification scheme derived optically from NASA's Moderate Resolution Imaging

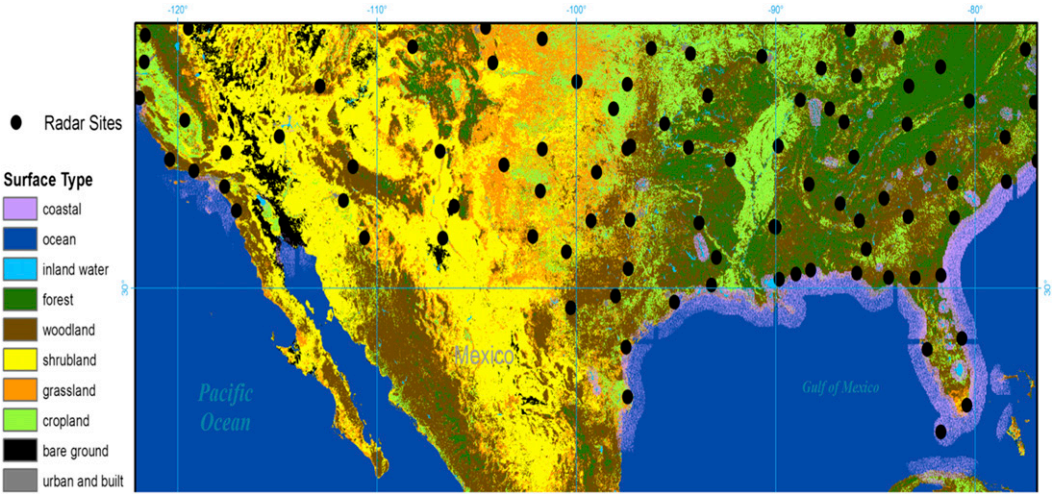

FIG. 1. Study domain showing the surface classifications. Note coastal and ocean classifications come from TRMM while the land classification is derived from MODIS. The grassland and shrubland categories were combined into a single class as well as the woodland and forest categories. The black dots represent reference radar locations.

Spectroradiometer (MODIS) is employed, in conjunction with the native three-category TRMM classification (Friedl et al. 2010).

Details regarding the study domain, the surface classification procedure, the satellite precipitation product 2A12, and the reference rainfall dataset are presented in section 2. Section 3 assesses 2A12's ability to detect, characterize, and quantify rainfall as a function of surface and precipitation characteristics. Concluding remarks and suggestions for future research are provided in section 4.

2. Data sources

To evaluate the influence of surface and precipitation characteristics on TMI 2A12 rainfall estimates, the 2A12 rainfall estimate $R(A)$ is compared with a reference rainfall estimate $R_{\text{ref}}(A)$ over a spatial domain A (the TMI footprint at the resolution of the 85-GHz channel) at the snapshot (i.e., rain rate) time scale. Results from these comparisons are then linked to precipitation properties such as spatial structure and classification. The results are also linked to surface characteristics through a surface classification scheme. This section details the study domain, the surface classification scheme, the reference precipitation products, and the satellite precipitation products.

a. Study domain

Because of the infrequent sampling of LEO satellites like TRMM (Wolff and Fisher 2008, 2009; Lin and Hou 2008), a large number of overpasses is required to get a sufficient number of coincident measurements from ground and space; consequently, this study utilizes seven months (March–September 2011) of satellite overpasses over the southern continental United States (CONUS; south of ~38°N) and nearshore ocean. This area, along with the reference ground radar sites, is shown in Fig. 1. All rain fields observed coincidentally by TRMM overpasses and the WSR-88D network during the time period are utilized in the following analysis. The dataset is limited spatiotemporally to primarily warm-season and liquid precipitation; however, this limitation is not too significant because current ground radar and PMW sensors are not well equipped to quantitatively estimate frozen precipitation (Moisseev et al. 2009). Also, a detailed evaluation of PMW retrievals over the midlatitudes is particularly pertinent given the recent launch of the GPM core satellite (which will also cover the midlatitudes). The dataset includes deep convection common to the southern portion of the United States during the warm season as well as a variety of mesoscale and synoptic weather systems such as tropical cyclones, orographic rainfall, and frontal precipitation.

b. Surface type classification

To examine the effects of surface characteristics on TMI retrievals, a multistep surface classification procedure was employed, which partitions the study domain on the basis of both TRMM and MODIS data. The first step of the classification procedure utilizes 2A12's native surface type variable to classify areas in the study domain as land, ocean, or coast. This initial partitioning was performed to separate biases related to algorithm differences (a different retrieval methodology is applied over each of

TABLE 1. The total number of TMI reference data pairs for each surface type, as well as the number of data pairs in which one or both sensors detect precipitation (i.e., >0).

Surface type	No. of data pairs	No. of reference >0 and TMI >0	No. of reference >0	No. of TMI >0
Cropland	287 911	78 199	279 265	85 239
Grassland	290 187	52 694	264 987	75 151
Woodland	1 029 824	308 814	1 002 645	330 205
Inland water	19 894	5325	17 919	7173
Ocean	682 399	205 400	253 145	633 187
Coast	423 176	78 922	412 109	85 576

these surface types), from those related to surface characteristics. Once this initial classification was performed, areas classified as land were further divided into eight MODIS-classified categories: bare ground, urban, grassland, shrubland, cropland, woodland, forest, and inland water (Fig. 1). The more qualitative MODIS classification was chosen over explicit soil moisture and vegetation fraction and skin temperature sources primarily for the following reasons: the use of the MODIS categories limits the amount of data sources incorporated in the study, as the MODIS categories summarize a number of surface characteristics, and this study is meant to provide a first look at the influence of surface properties on PMW precipitation retrievals. Consequently, future studies will incorporate more quantitative sources.

For every pixel identified as land in step 1, the surface type of each TRMM–Q2 data pair was determined by spatially matching the center of the TMI pixel with the aforementioned classification dataset. All pixels identified as coastal or ocean in step 1 were left as separate categories and were not matched with the MODIS dataset. The final processing step was aggregating several (physically) similar categories to improve data robustness and eliminating categories containing insufficient samples. Specifically, the woodland and forest categories were combined as well as the grassland and shrubland categories. These new aggregated categories are referred to hereafter as woodland and grassland. The bare ground and urban categories were not considered in the following analysis because of an insufficient number of raining [both $R_{\text{ref}}(A)$ and $R(A)$ positive] samples (353 for bare ground and 3274 for urban). After these processing steps, the number of land surface type categories analyzed was thus reduced to three (ordered here by increasing average soil moisture content/vegetative fraction): grassland, cropland, and woodland. The MODIS-classified inland water category was also included in the analysis (note most of the inland water bodies are classified by 2A12 as land and thus rain rates are retrieved with the land algorithm despite the fact that emissivity over inland water bodies is considerably different); however, it must be noted that because of the relatively small spatial extent of most inland water bodies in the study domain and the relatively large size of the TMI pixel, it is possible that many pixels classified as inland water contain effects from adjacent surface types. Finally, the pixels originally classified by 2A12 as coastal and ocean are also included in the analysis. However, because of the limited effective range of the reference ground radars, data pairs classified as ocean are limited to those areas within ~200 km from near-coastal radar locations, and thus the over-ocean dataset may not be representative of typical oceanic conditions (although the ocean retrieval algorithm is employed). It is also important to recognize that 2A12 classifies the borders of some sizeable inland water bodies as coastal (Fig. 1), and thus not all coastal areas necessarily represent transition zones between the land and ocean algorithms. The second column of Table 1 provides the number of matched TMI–ground radar data pairs for each of the surface categories included in the analysis.

c. *Reference precipitation products*

The NOAA/NSSL Q2 system (http://mrms.ou.edu; Zhang et al. 2011a) is a set of experimental radar products including high-resolution (0.01°, 5 min) instantaneous rain-rate mosaics available over the CONUS. The Q2 system assimilates information from all ground-based radars comprising the WSR-88D network [Next Generation Weather Radar (NEXRAD); sites shown in Fig. 1], mosaics reflectivity data onto a common 3D grid, and estimates surface precipitation type and amount (Zhang et al. 2005; Lakshmanan et al. 2007; Vasiloff et al. 2007; Kitzmiller et al. 2011). In addition, Q2 adjusts radar estimates with rain gauge networks at hourly time steps, and a radar quality index (RQI) is associated with the radar QPE estimates and takes into account uncertainties arising from vertical variations of reflectivity (Zhang et al. 2011b). A simplified stratiform–convective classification scheme is applied by utilizing the vertically integrated liquid (VIL) content derived from the Q2 3D mosaics at the original resolution (1 km, 5 min) and follows a two-step approach similar to Steiner et al. (1995) to identify convective areas (Kirstetter et al. 2015).

Radar QPE is potentially subject to numerous sources of error, namely, nonweather echoes, vertical profile of

reflectivity (VPR) variability, conversion of radar reflectivity to rain rate, and calibration of the radar signal. While several procedures are already in place within the Q2 system to correct for these errors, post-processing was used to further refine the reference dataset by adjusting and quality-controlling instantaneous radar-only products using the RQI and collocated rain gauge observations. Hourly biases were computed between collocated rain gauges and radar-only estimates and subsequently applied downscale to adjust the instantaneous rain-rate estimates. A conservative approach was followed by filtering out instances when the radar and gauge have significant quantitative disagreement (i.e., radar–rain gauge ratios outside of the range 0.1–10). This adjustment is designed to minimize uncertainties associated with the rain rate–reflectivity relationship and calibration errors [see Kirstetter et al. (2012) for more details]. The RQI further filters out measurements affected by beam blocking and overshooting (i.e., radar beam above the melting layer). These quality-control processes also standardize the reference product, which is significant because ground radar measurements in the Intermountain West tend to be of lower quality than measurements from other regions of the country. Even following this rigorous processing procedure, some errors may still exist in the ground-based radar estimates of rainfall, thus preventing the strict validation of 2A12 surface precipitation estimates.

d. Satellite-based (2A12) precipitation products

The TMI measures brightness temperatures at five microwave frequencies: 10.7, 19.4, 21.3, 37.0, and 85.5 GHz. Both the horizontal H and vertical V polarizations at each frequency are measured, except for the 21.3-GHz channel, in which only the vertical is measured. The calibrated brightness temperatures are used as inputs for the 2A12 (rain-rate estimation) algorithm. Over the land, the algorithm used to retrieve surface rainfall is described in McCollum and Ferraro (2003), Wang et al. (2009), and Gopalan et al. (2010); the ocean algorithm is described in Petty (1994), Kummerow et al. (2001), and Kummerow et al. (2011); and the coastal algorithm is described in McCollum and Ferraro (2005). The algorithms are briefly summarized below.

The ocean algorithm relates the full vector of retrieved brightness temperatures, with a database of hydrometeor profiles in a Bayesian framework to estimate rain rates (Kummerow et al. 2001, 2011) and other cloud and precipitation properties (such as convective–stratiform classification). The land algorithm calculates rain rates through empirically derived rain rate–85V Tb relationships and applies distinct rain rate–Tb relationships for convective and stratiform precipitation. The convective–stratiform rain fraction for every pixel is obtained by utilizing the 10-GHz vertically polarized Tb (10V Tb), 37-GHz vertically polarized Tb (37V Tb), and 85-GHz horizontally (85H Tb) and vertically (85V Tb) polarized Tb and is based on assumed relations between the magnitude and spatial structure of Tb depressions, precipitation microphysics, environmental factors, and precipitation type, that is, stratiform or convective (McCollum and Ferraro 2003; Grecu and Anagnostou 2001; Prabhakara et al. 2000; Olson et al. 2001). Because of the classification algorithm's use of lower-frequency channels (which experience less attenuation by hydrometeors then the higher-frequency channels), it is more susceptible to variations in surface properties and consequently represents a way for the surface to influence the precipitation retrievals. Following classification, the total rain rate for the pixel is then estimated through weighted averaging using the estimated convective fraction, and consequently, the classification and quantification components of the overland algorithm are strongly linked. For version 7 of the 2A12 land algorithm, the empirical basis for the rain rate–Tb relationships and precipitation classification is primarily TRMM PR data (the 2A25 and 2A23 products, respectively; Gopalan et al. 2010). The current version of the coastal algorithm simply performs a weighted average of the ocean and land precipitation retrievals and attempts to prevent discontinuities between ocean and land estimates (McCollum and Ferraro 2005).

Overland and coastal PMW precipitation estimates rely primarily on 85V Tb depressions resulting from microwave scattering by frozen hydrometeors. Because frozen hydrometeors (particularly in the warm season/lower latitudes) generally reside in the mid- to upper troposphere, this information may not be representative of surface precipitation, adding uncertainty to surface rain-rate estimates (Wilheit et al. 2003). Because of the similarities between Tb depressions associated with sand-covered and frozen surfaces and those associated with scattering by frozen hydrometeors, a surface screening procedure is employed to limit false alarms and/or precipitation overestimation over such surfaces. This precipitation mimicking effect is also seen to a lesser degree over dry and sparsely vegetated regions, often resulting in 2A12 overestimating precipitation over these areas, as noted by Wang et al. (2009) and Gopalan et al. (2010). Because of its reliance on the scattering signature produced by ice, 2A12 also tends to significantly underestimate overland precipitation resulting from "warm rain" events [defined as precipitation events consisting of primarily liquid-phase hydrometeors (Liu and Zipser 2009)].

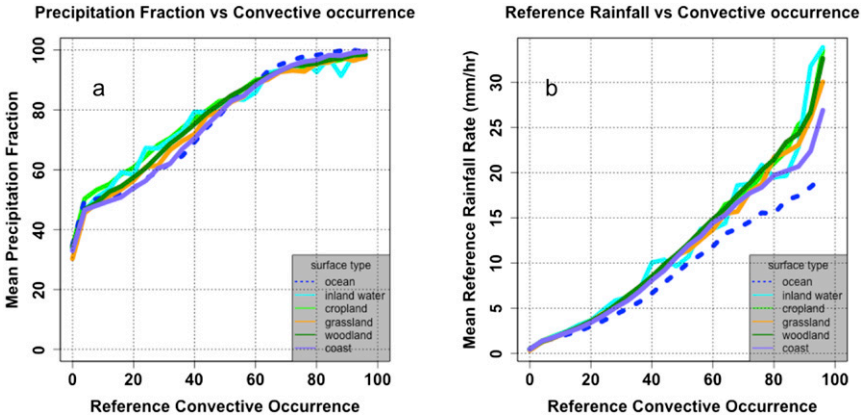

FIG. 2. Reference convective occurrence plotted against mean reference (a) PF and (b) rain rate.

e. *Comparison samples*

The Q2 products closest in space and time to the TRMM satellite's local overpass time are used in the following analysis. The reference rainfall unconditional mean quantities were computed by aggregating the Q2 pixels (rainy and nonrainy) within the TMI pixel A. The mean number of Q2 sample points (with the native Q2 QPE product resolution being $1\,\mathrm{km}^2$) associated with each satellite pixel is 170. When more than 25% of the Q2 pixels have missing values over a specific pixel A, this sample point is discarded from the comparison to preserve the reliability and representativeness of the block-Q2 and 2A12 values. Matched 2A12 and $R_{\mathrm{ref}}(A)$ estimates only exist at locations where both the TMI and ground radars have taken actual observations. This technique allows the satellite products to remain untouched, allowing for the preservation of some of their important characteristics, including the rainfall amount, the raining area, the convective–stratiform contribution, and the PDF shapes. These characteristics may thus be compared to the reference immediately without any spatiotemporal interpolation. The reference rainfall is further described in terms of its spatial structure and classification within the satellite pixel though the following derived products.

(i) The precipitation fraction PF (Fig. 2) describes the rainfall occurrence within the 2A12 pixel and represents as the proportion of positive (rain rate $> 0\,\mathrm{mm\,h^{-1}}$) Q2 pixels inside the 2A12 pixel. It is expressed in percent between 0% (no raining Q2 pixels within the TMI pixel) and 100% (all Q2 pixels raining within the TMI pixel).

(ii) The convective occurrence (Fig. 2) classifies the rainfall as the proportion of Q2 pixels classified as convective. It is expressed in percent between 0% (stratiform—no convective Q2 pixels within the TMI pixel) and 100% (convective—all Q2 pixels classified as convective within the TMI pixel).

(iii) The convective volume fraction CVF quantifies the contribution of convective rainfall to $R_{\mathrm{ref}}(A)$ as follows:

$$\mathrm{CVF}(A) = 100\,\frac{\sum_{j=1}^{n_{\mathrm{conv}}} \mathrm{Q2}(a_j)}{\sum_{i=1}^{n} \mathrm{Q2}(a_i)}, \tag{1}$$

where $\mathrm{Q2}(a_j)$ denotes the Q2 rain rate at the original data product resolution ($1\,\mathrm{km}^2$) a_i, n is the number of Q2 data points inside the common grid pixel A, and $n_{\mathrm{conv}} \le n$ is the number of Q2 pixels flagged as convective inside the pixel A. Note that each 2A12 pixel is associated with a rain rate at ground and with an associated convective rain rate. As for Q2, the CVF is computed to quantify the contribution of convective rainfall to $R(A)$.

Several factors such as rainfall intermittency, discrete temporal sampling of TRMM, and censoring of reference values for required quality reduce the number of comparison samples for reference and satellite estimates over the domain and comparison period. Our data sample consists of 2 733 391 matched data (satellite and reference) inclusive of nonrainy pixels (either the reference or satellite is equal to zero). Details on the data sample are provided in Table 1.

More insight into the reference rainfall characteristics is provided in Fig. 2. Relationships between the reference rainfall characteristics, that is, PF, CVF, and reference rain rate, are shown for each surface type. The

TABLE 2. Contingency table statistics for 2A12 relative to the reference for each surface type.

Surface type	H (%)	M (%)	F (%)	C (%)	POD	FAR	CSI	MVOL	FVOL
Cropland	27.2	69.8	2.4	0.6	28	8	27	26	3.03
Grassland	18.2	73.2	7.7	0.9	20	30	18	32.1	8.45
Woodland	30	67.4	2.1	0.6	31	6	30	19.9	2.82
Inland water	26.8	63.3	9.3	0.6	30	26	27	21.2	6.56
Ocean	30.1	7	62.7	0.2	81	68	30	4.2	11.4
Coast	18.6	78.7	1.6	1	19	9	19	34.4	3.65

rain fraction increases with the convective occurrence from ~30% for purely stratiform reference rainfall up to 100% for convective reference (Fig. 2a). The first case is likely associated with incipient or decaying precipitation systems or those located near the boundaries of rainfall fields sampled within the TMI footprint, while the latter case likely corresponds to more extensive and organized convective systems. Values of PF over the coast or ocean are slightly lower than over the land for primarily stratiform cases (convective occurrence in the range of 10%–50%) and slightly higher for primarily convective cases (convective occurrence greater than 70%). The average reference rainfall is also an increasing function of the convective occurrence, as expected (convective systems tend to be associated with more intense vertical motions and precipitation growth processes). Precipitating systems tend to generate higher mean rain rates over the land compared to coastal areas in primarily convective events (>70% convective occurrence) and ocean for all amounts of convective occurrence (Fig. 2b).

3. Rainfall data analysis

This section evaluates the ability of TMI 2A12 to detect (section 3a), classify (section 3b), and quantify (section 3c) surface precipitation relative to reference precipitation products as a function of both surface and precipitation characteristics.

a. Rainfall detection

Table 2 displays contingency statistics that detail the satellite's ability to detect precipitation relative to the reference, with percentage of hits H (both reference and satellite have nonzero rainfall amounts), misses M (satellite has zero rain while the reference has nonzero amounts), false alarms F (satellite has nonzero rain while the reference amount is zero), and correct rejections C (both reference and satellite have zero rain) provided for all surface types. Derived metrics such as probability of detection POD = $100[H/(H + M)]$, false alarm rate FAR = $100[F/(H + F)]$, critical success index CSI = $100[H/(H + M + F)]$, missed volume of rainfall MVOL, and volume associated with false alarms FVOL are also provided in Table 2. To graphically highlight the sensor's detection capabilities, Heidke skill score HSS, POD, and FAR for all surface types are calculated and plotted against reference or 2A12 rain-rate estimates (Figs. 3, 4). To evaluate the influence of precipitation characteristics on 2A12's detection capabilities, POD as a function of reference precipitation fraction and convective occurrence is also plotted (Figs. 4b,c). The impacts of precipitation detection on TMI's quantification of precipitation will be discussed in section 3c.

Over the land, TMI 2A12 misses a significant portion (63%–73%) of the reference rainfall occurrence and volume (20%–32%; Table 2). The high number of missed events likely results from TMI's lower sensitivity relative to the reference, a result of both its coarser spatial resolution and the reliance of its detection capabilities on a developed ice phase. TMI 2A12's detection capabilities improve with increasing (average) vegetation fraction and (average) soil moisture content. This is best seen via an increase in CSI from 18 over grassland (the most arid category) to 27 over cropland and up to 30 over woodland (the most vegetated surface). This increase in CSI results from both an increase in the POD and a decrease in the FAR. The high FAR (30 compared to 6 over woodland) over grassland likely results from the arid surface signal mimicking the scattering signal associated with frozen hydrometeors (section 2d). The low POD over the grassland category could be a result of the surface screening procedure screening out some very low vegetated/sand-covered surfaces where precipitation is actually occurring. However, another explanation is that the poor detection capabilities result from the typical characteristics of precipitating systems in the region (which is primarily located in the Intermountain West). Specifically, shallow orographic precipitation and isolated (the mean precipitation fraction for all raining events over grassland is 9% lower than any other category) events are common over this category, and TMI has been known to have difficulty detecting these types of precipitation because of their limited ice content and spatial extent (Shige et al. 2013). However, a more detailed evaluation of precipitation properties would be required to evaluate this hypothesis.

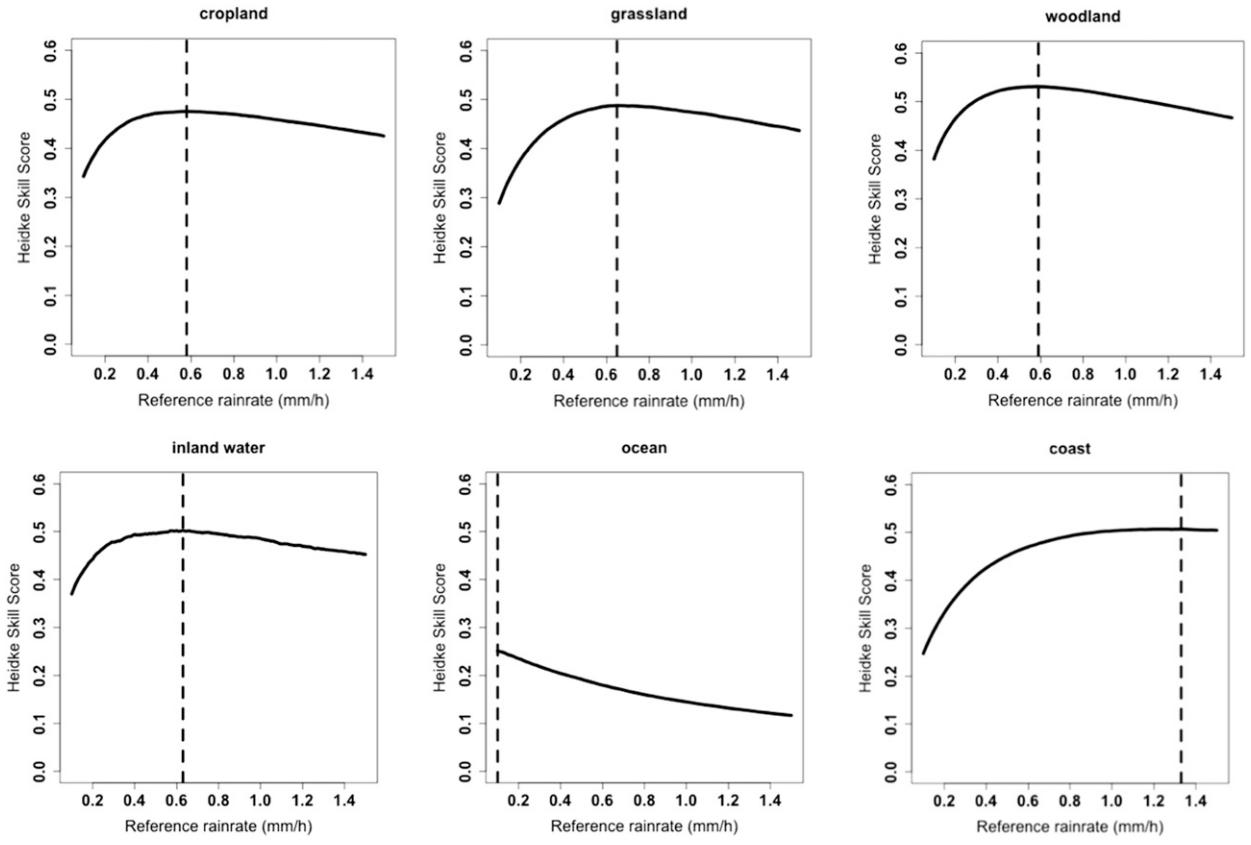

FIG. 3. Plots of HSS for all surface types where the vertical dotted line corresponds to the reference rain rate associated with the max HSS and thus represents an approximate detection threshold.

TMI 2A12's detection capabilities over inland water are more difficult to evaluate, given the relatively low number of data pairs (Table 1). However, the high FAR (26) could result from surface influences, as the surface microwave emissivity of inland water is considerably different than over the land. This result is similar to the findings of Tian and Peters-Lidard (2007), who found an abundance of false alarms in the level 3 (merged sensor) TRMM products, and thus, this could potentially represent an occurrence of error propagation between the level 2 (one sensor snapshot scale) and the level 3 products (multisensor/longer time scale).

Over the coastal areas, TMI 2A12 misses an even greater portion of the reference rainfall (78.7% of occurrence and 34% of volume), and consequently, the POD is the lowest of any category (Table 2). The large quantity of misses likely results from the conservative decision tree approach utilized by the coastal algorithm (McCollum and Ferraro 2005), which imposes a series of thresholds that must be exceeded before a pixel is classified as raining (or rain ambiguous). While this conservative approach results in a high number of missed precipitation events, it is likely (currently) necessary to prevent excessive false alarms resulting from the large gradients of surface emissivity present within coastal pixels.

Over the ocean, TMI 2A12's detection behavior is quite different than over the land/coast, and specifically, the POD (81) and FAR (68) are by far the highest of any category (Table 2). This is primarily a result of the different retrieval algorithm applied over the ocean, which does not apply a simple rain/no-rain mask to each pixel. Instead, the retrieved brightness temperatures are matched in a Bayesian framework with hydrometeor profiles from the retrieval database [which is developed using PR vertical profiles and cloud-resolving model simulations; see Kummerow et al. (2011) for more information], and if any of these profiles are associated with nonzero rain rates, the pixel is assigned a nonzero rain rate (Kummerow et al. 2001). Therefore, over the ocean a probability of precipitation (based on the proportion of matched profiles with positive rain rates) is instead provided for each pixel, and it is the responsibility of the end user to create an appropriate rain/no-rain threshold based on these probabilities. The probabilities of precipitation were not included in the current study, and consequently, the vast majority

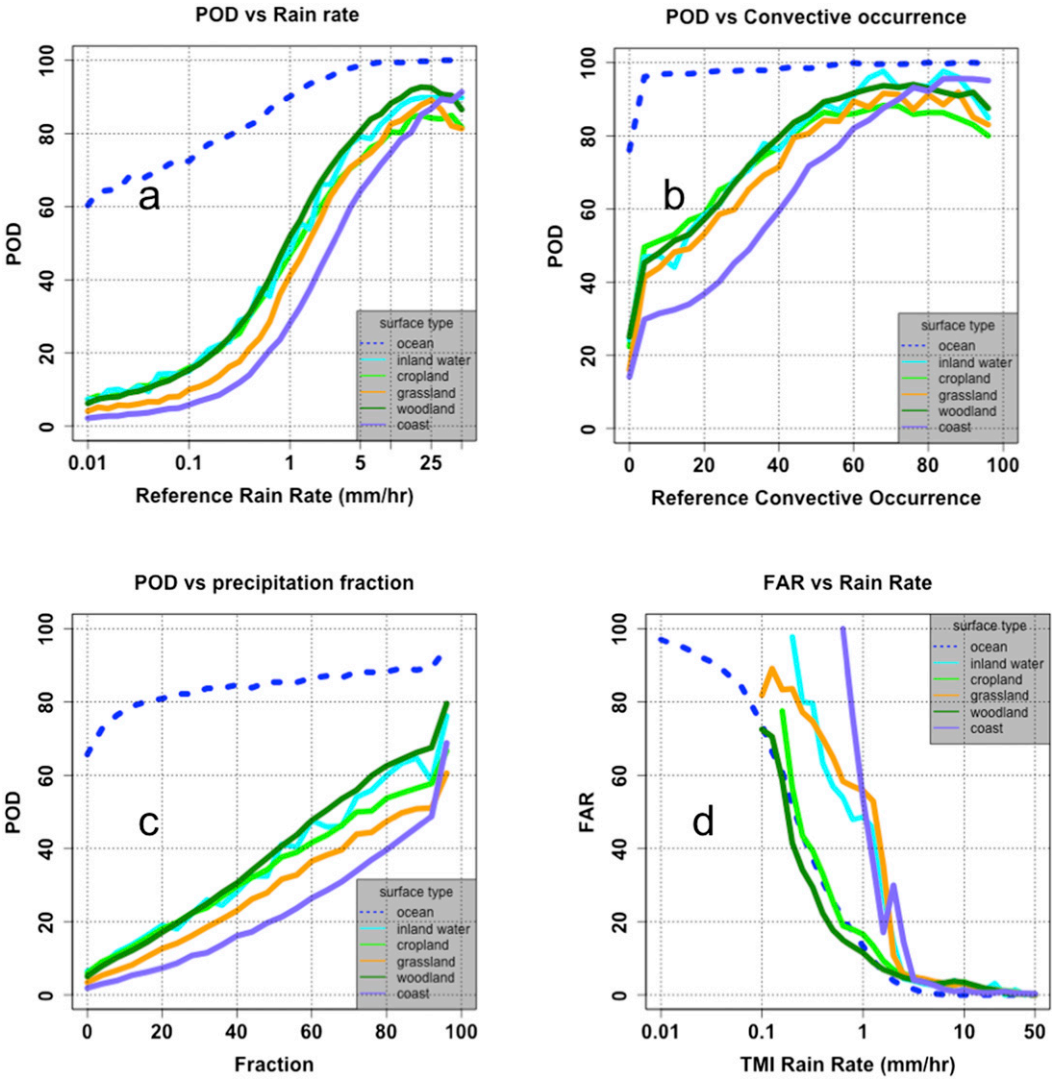

FIG. 4. The 2A12 POD as a function of (a) reference rain rate, (b) reference convective occurrence, (c) PF, and (d) 2A12 FAR as a function of TMI rain rate.

(92.7%) of ocean pixels contains nonzero 2A12 rain-rate estimates. This results (using our detection criteria) in the ocean algorithm detecting almost all precipitation, but also results in copious amounts of false alarms. So, while it would be expected given the same detection scheme, the ocean algorithm would display improved detection capabilities (because it is not reliant on a developed ice phase), and the detection capabilities are also artificially increased by the nature of the retrieval scheme. Consequently, it is very difficult to evaluate the detection capabilities of the ocean algorithm with this methodology, and a rigorous assessment would require analyzing the probability of a precipitation variable.

The HSS shown in Fig. 3 provides a quantitative measure of TMI 2A12's skill in detecting precipitation relative to random chance. Maximizing the HSS enables us to identify the approximate detection threshold for the sensor (Wolff and Fisher 2009; Wilks 2011). An HSS score of 1 indicates a perfect delineation between TMI 2A12 detection (relative to the reference) above some threshold and missed precipitation below it, while a score of zero indicates no skill (note that negative values can exist and would actually imply the sensor's detection capabilities are worse than a random guess). The HSS is defined as (Brier and Allen 1952)

$$\mathrm{HSS} = \frac{2(HC - FM)}{F^2 + M^2 + 2HC + (F + M)(H + C)}. \quad (2)$$

Over all land categories the detection thresholds (represented by the dashed line) are relatively similar ($\sim$0.6 mm h^{-1}); however, the maximum HSS increases

TABLE 3. Contingency table statistics for 2A12 relative to the reference for each surface type for convective precipitation.

Surface type	*H* (%)	*M* (%)	*F* (%)	*C* (%)	POD	FAR	CSI
Cropland	24.60	12.90	7.60	54.80	65.00	24.00	54.00
Grassland	26.70	8.60	12.40	52.30	76.00	32.00	56.00
Woodland	26.10	11.90	8.30	53.70	69.00	24.00	56.00
Inland water	24.10	12.30	7.80	55.80	66.00	24.00	55.00
Ocean	32.30	0.40	66.80	0.50	99.00	67.00	32.00
Coast	45.90	0.00	54.10	0.00	100.00	54.00	46.00

with average vegetative fraction and soil moisture. Because of the stringent rain/no-rain mask applied to coastal pixels, the detection threshold is quite high ($\sim$1.4 mm h^{-1}), while the opposite is true over the ocean, where some precipitation is nearly always detected (due to the retrieval algorithm).

Over all surface categories, TMI 2A12's detection capabilities increase markedly with increasing reference rain rate and convective occurrence (Figs. 4a,b). This likely occurs because of a more pronounced ice-scattering signal associated with (deep) convection and high rain rates. Therefore, it is possible that many of the misses at higher rain rates are associated with warm rain/shallow precipitation events; however, more detailed information regarding the precipitation's microphysical properties and the meteorological environment would be required to confirm this. TMI 2A12's detection capabilities are also positively correlated with reference precipitation fraction (Fig. 4c). This is primarily a consequence of the large size of the TMI pixel, which causes signals arising from small-scale/isolated precipitation features (which correspond to a low precipitation fraction) to be largely obscured by the signal arising from nonprecipitating parts of the pixel. It must be noted, however, that because of the connections between convective occurrence, precipitation fraction, and rain rate (Figs. 2a,b), it is difficult to isolate their individual effects on TMI 2A12's detection capabilities. The FAR also decreases with TMI 2A12 rain rate (Fig. 4d), since the magnitude of the radiative signatures that result in false alarms (such as orphan anvils associated with decaying convection and surface emissivity effects) tends to be relatively low compared to the ice-scattering signatures usually associated with high rain rates.

b. Rainfall classification

Precipitation classification by PMW sensors can have significant impacts on their precipitation estimates, and specifically, (the over land) version 7 of 2A12 applies distinct rain rate–Tb relationships for stratiform and convective precipitation. Although not detailed in this study, accurate precipitation classification is also important for the estimation of latent heating profiles, which are important for many meteorological applications (Olson et al. 2001). In this section, we evaluate the ability of 2A12 to detect and quantify convection relative to the reference, while the impact of classification on 2A12's precipitation estimates is detailed in the following section (section 3c). To eliminate issues related to precipitation detection, only cases when both 2A12 and the reference rainfall are greater than zero are considered in this section. It must be noted here that partitioning of precipitation into convective and stratiform categories using remote sensing methods is inherently subjective; however, since the empirical basis for 2A12's precipitation classification algorithm is the TRMM PR (a radar), evaluating the algorithm with another (independent) radar-derived classification product seems logical.

The definitions of the reference convective volume and 2A12 convective volume fraction variables were provided in section 2e. It is important to note that the 2A12 CVF estimate is inherently probabilistic in nature [see Gopalan et al. (2010) for more information], and therefore, 2A12-estimated convective fractions very rarely reach 100%. Consequently, in the following analysis, 2A12 convective fractions over 90% are taken to represent pure convective precipitation (according to the sensor). Despite these slight differences between the reference and 2A12 convective volume products, they both provide estimates of the convective contribution to the total precipitation volume within the TMI footprint and thus make it possible to (somewhat) quantitatively compare the two sensors' classification algorithms.

Table 3 details the satellite sensor's ability to detect convective precipitation relative to the reference and is nearly identical in form to Table 2, with precipitation replaced by convective precipitation (i.e., a hit in this situation occurs when both the reference and 2A12 detect convective precipitation). Values of POD and FAR for all surface types are also plotted against reference and 2A12 CVFs, respectively (Figs. 5a,b).

2A12's ability to detect convection is relatively similar over all land categories, although a higher percentage of false alarms (12.40%) is noted over the more arid grassland surface (Table 3), once again a probable result of significant Tb depressions arising from the surface signal (which mimics the ice-scattering signal

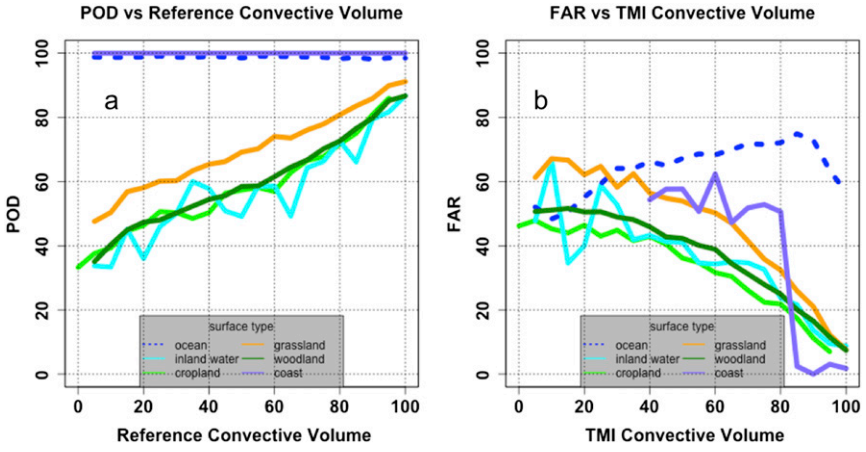

FIG. 5. (a) The 2A12 convective POD as a function of reference convective volume and (b) the 2A12 convective FAR as a function of 2A12 convective volume.

produced by convective precipitation). This may also explain the higher POD (76.00) over grassland, as the surface signal amplifies the ice-scattering signal, enabling the classification algorithm to ''correctly'' classify weaker convection. As expected, over all land categories, 2A12's convective detection capabilities increase with increasing reference and TMI 2A12 convective volume fractions (Figs. 5a,b).

A quantitative evaluation of the coastal and ocean classification algorithms is difficult because the coastal and ocean classification algorithms nearly always detect at least some convective precipitation. This is largely due to the nature of Bayesian retrievals, in which the use of prior data is combined with the observed data to produce posterior parameter estimates. Naturally, a fairly substantial number of the hydrometeor profiles composing the prior database include at least some convective precipitation, and therefore, the final retrievals will contain some convective artifacts simply because of the mechanics of the retrieval. Coastal pixels are also impacted by the ocean classification scheme as their retrievals are a weighted average of the land and ocean portions within the pixel. This results in a very high (convective) POD (99 and 100) and FAR (67 and 54) over these surfaces (Table 3); however, as discussed in the detection section, these metrics are not well suited to evaluate this type of algorithm. The FAR over the coast appears to drop significantly at 2A12 convective volume fractions >80% (Fig. 5b); however, this is likely due to a scarcity of data at convective volume fractions greater than this point (to be elaborated on in the following section), rather than any actual improvement in convection detection.

Table 4 and Fig. 6 detail the satellite sensor's ability to quantify convection relative to the reference, with Fig. 6 displaying a density scatterplot that provides a visual comparison of the two sensors' classification algorithms and Table 4 providing a more detailed/quantitative breakdown of the same information. However, because of both the subjective nature of precipitation classification and the slight differences between the reference and 2A12 CVF variables, the following results are best

TABLE 4. Percent of data pairs from both sensors classified within the following categories: pure stratiform (CVF = 0%), primarily stratiform (CVF = 1%–50%), primarily convective (CVF = 51%–90%), and pure convective (CVF > 50%).

Surface type	Sensor	Pure stratiform (%)	Primarily stratiform (%)	Primarily convective (%)	Pure convective (%)
Cropland	TMI	67.8	6.2	15.8	10.2
	Q2	62.5	11.6	13.9	12.1
Grassland	TMI	60.9	7.5	19.8	11.7
	Q2	64.8	11.5	14.6	9.3
Woodland	TMI	65.6	6.1	16.6	11.7
	Q2	62.0	11.5	14.8	11.8
Inland water	TMI	68.1	6.0	15.5	10.4
	Q2	63.6	11.0	13.5	11.9
Ocean	TMI	0.9	31.2	63.5	4.4
	Q2	67.2	10.6	15.4	6.8
Coast	TMI	0.00	52.2	47.1	0.8
	Q2	54.1	6.4	18.2	13.1

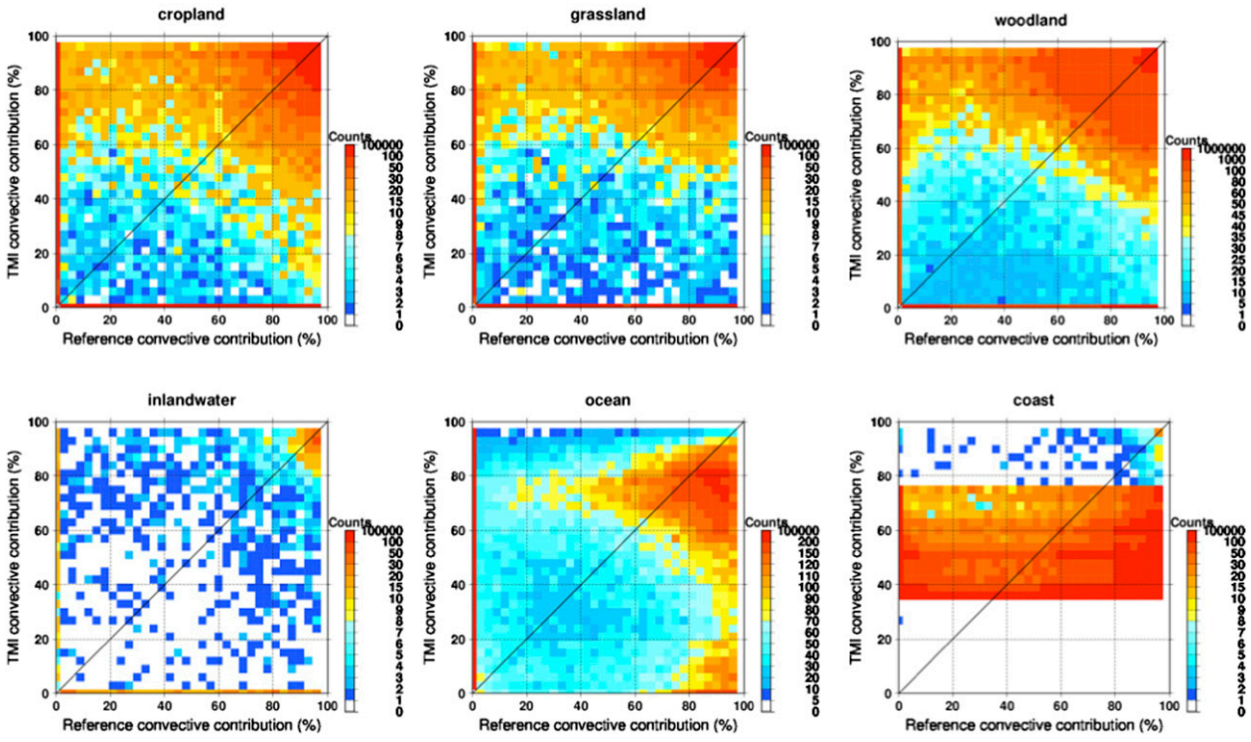

FIG. 6. Density-colored scatterplots of 2A12 convective volume vs reference convective volume for each surface type.

interpreted in a more general sense. Overland 2A12 captures the relative contributions of pure stratiform (CVF = 0%) and pure convective (CVF > 90%) precipitation well relative to the reference (Table 4). This is particularly remarkable when one considers the subjectivity of precipitation classification and the inherent uncertainties present in PMW classification algorithms. There are some slight discrepancies, however, primarily over the grassland surface where 2A12 tends to overestimate the amount of pure convective precipitation (11.7% compared to 9.2%), once again a probable result of the surface aridity. Over the land, the biggest classification discrepancies between the two sensors occur in mixed convective and stratiform precipitation events (which result in about 25% of the total rainfall volume). Specifically, 2A12 has a tendency to slightly underestimate the number of primarily stratiform events (CVF = 1%–50%) and slightly overestimate the number of primarily convective (CVF = 51%–90%) events relative to the reference (Table 4). These discrepancies are evident over all land surface types but are particularly amplified over grassland, where overassigning convective precipitation is consistently an issue (Fig. 6). These differences, while small in magnitude, may arise because of flaws within 2A12's overland classification algorithm, and specifically may result from the training dataset (TRMM PR) used to develop the algorithm. It seems probable that most of the cases utilized to develop the algorithm represented fairly pure (from a radar classification standpoint) convective or stratiform precipitation events, while mixed stratiform–convective precipitation events may have been underrepresented.

Over the ocean and coastal categories, 2A12 tends to overestimate convection considerably relative to the reference (with relative biases of 187% and 74%, respectively), and 2A12 classifies virtually no precipitation as purely stratiform over these surfaces (Table 4). Over the coastal regions, 2A12 classifies the vast majority of precipitation as 35%–80% convective (Fig. 6), a result of the weighted averaging applied between the land and ocean retrievals (and the ocean retrievals nearly always detect convection). Over the ocean, 2A12 and the reference agree relatively well on the relative occurrence of pure convective precipitation, but differ considerably over all other categories, which is likely a result of the considerably different retrieval techniques employed by the reference and the sensor (i.e., radar-derived precipitation classification is likely to produce different results than the Bayesian profile matching approach utilized by TMI over the oceans).

c. *Rainfall quantification*

To investigate the ability of 2A12 to quantify surface precipitation (relative to the reference) the mean relative

TABLE 5. Conditional/unconditional MREs and CCs for each surface type.

Surface type	MRE (%) (Q2 and TMI >0)	Unconditional MRE (%)	CC
Cropland	30	−1	0.59
Grassland	61	20	0.59
Woodland	27	5	0.61
Inland water	26	7	0.61
Ocean	−28	−22	0.56
Coast	19	−18	0.54

error MRE [expressed in percentage and defined as $\mathrm{MRE} = 100(\overline{R_{\mathrm{ref}}} - \overline{R})/R_{\mathrm{ref}}$] and correlation coefficient CC were calculated over all surface types and are listed in Table 5. Two MREs were calculated, one in which errors related to detection were ignored [i.e., required $R_{\mathrm{ref}}(A)$ and $R(A) > 0$] and one in which this condition was removed. Scatterplots are also provided to highlight the general relationship between the 2A12 and reference precipitation estimates for each surface type (Fig. 7).

Over all nonocean surfaces, the conditional (on both sensors detecting precipitation) MRE is positive and increases with decreasing average soil moisture/vegetation fraction (ranging from 61% over grassland to 27% over woodland; Table 5). This general overestimation of precipitation over the land likely results from the overestimation of convective fraction by 2A12, and Fig. 8 displays the relationship (overland) between classification and quantification quite clearly. Specifically, the vast majority of points to the left of the 1:1 line [i.e., $R(A) > R_{\mathrm{ref}}(A)$] correspond to points where 2A12 overestimated the CVF relative to the reference (colored red) and vice versa for points to the right of the 1:1 line. The overestimation of convection is magnified over the arid grassland surface where the surface signal results in a large number of convective false alarms (Tables 3, 4). Over the ocean, the MRE is negative despite the tendency of 2A12 to drastically overestimate the convective contribution of precipitation (Tables 4, 5). This underestimation likely occurs because of a number of factors that act to smooth out very high rain rates, particularly the Bayesian framework employed by the retrieval algorithm (in which low prior probabilities are given to high rain rates), the large size of the TMI pixel, and the tendency of the retrieval channels to saturate at very high rain rates. It is also evident from Fig. 8 that, because of the greater robustness and sophistication of the over-ocean algorithm (which can utilize more

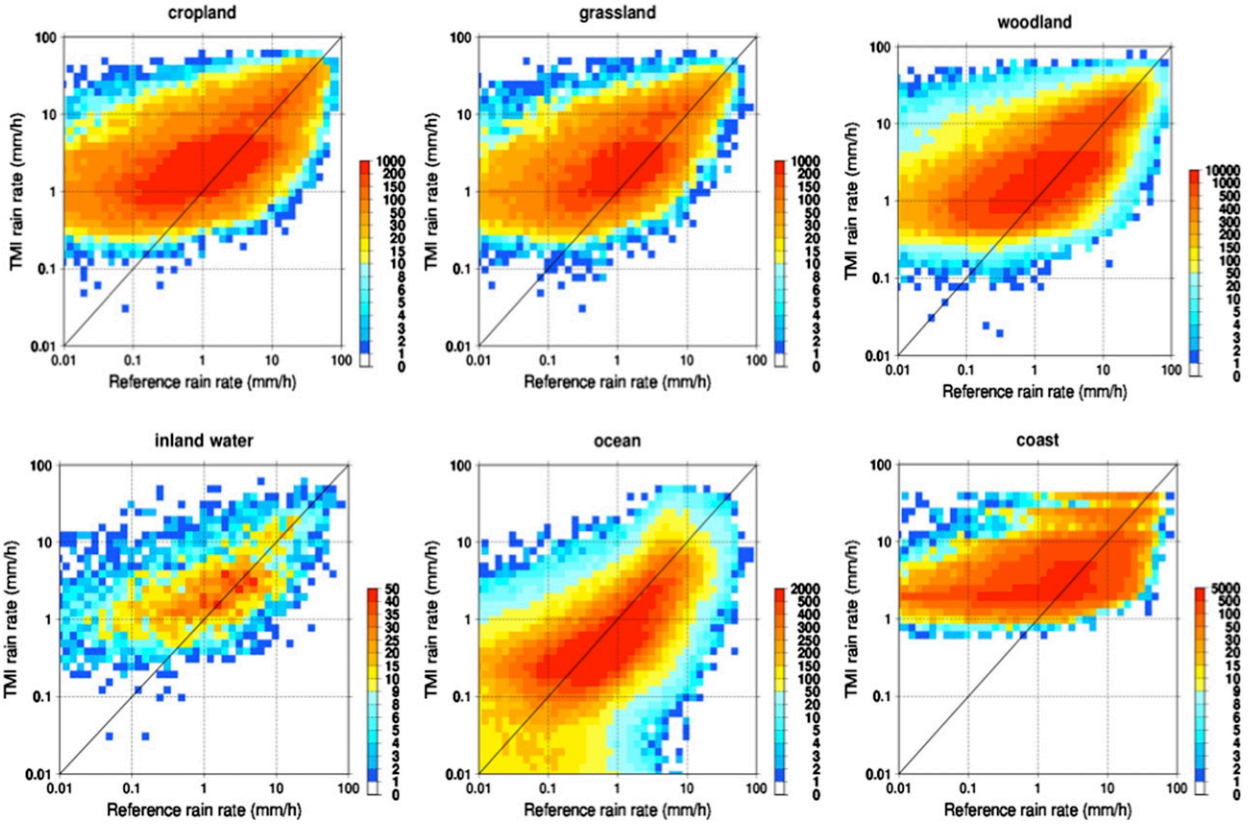

FIG. 7. Density-colored scatterplots of TMI rain-rate estimates vs reference rain-rate estimates for each surface type.

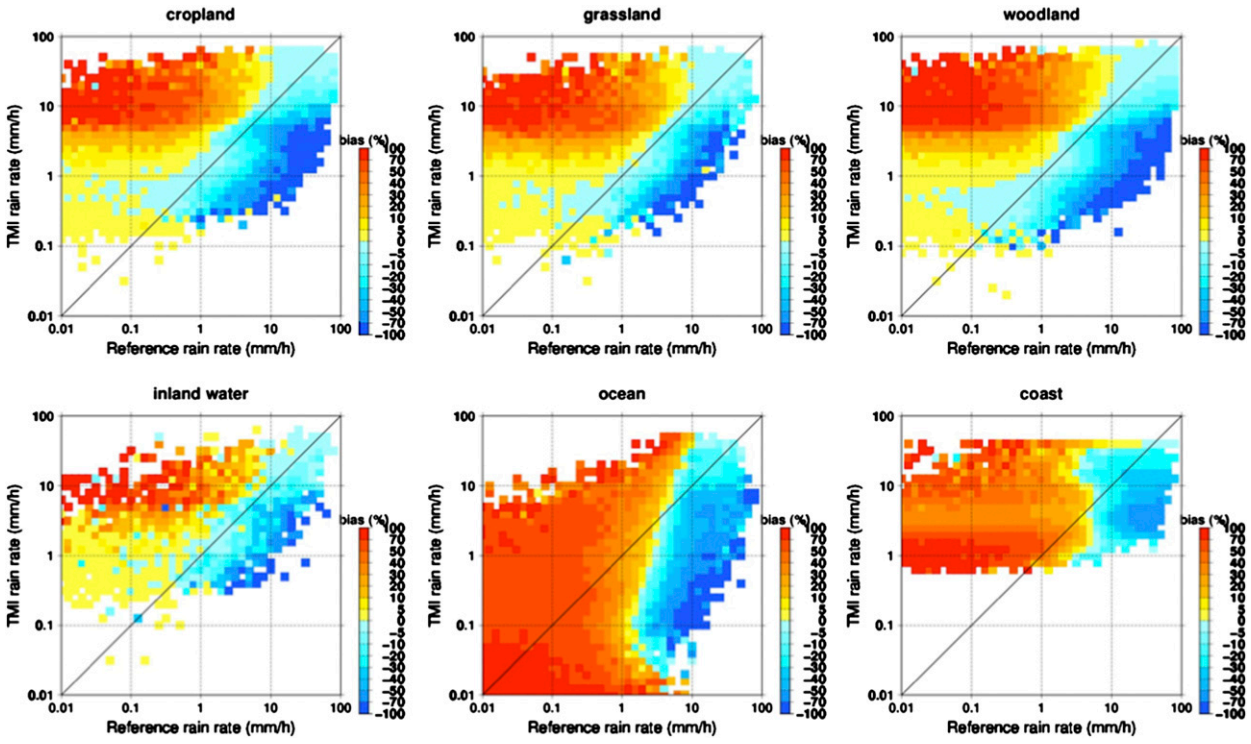

FIG. 8. Scatterplots of 2A12 rain-rate estimates vs reference rain-rate estimates for each surface type with the points colored according to the convective bias (2A12 convective volume minus reference convective volume).

channels in the retrieval process and is less reliant on a developed ice phase), over-ocean precipitation estimates are not as dependent on the classification algorithm. Over the coastal areas, the MRE is intermediate between land and ocean, which is expected given the nature of the coastal retrieval algorithm (section 3b).

When detection is taken into account, the MRE for all surfaces except ocean decreases because of 2A12's generally lower sensitivity relative to the reference [i.e., the number of missed events is considerably higher than false alarms (Table 2)] and the magnitude of the change in MRE over each surface is inversely proportional to the ability of the sensor to detect precipitation over that surface (Table 5). Specifically, the biggest decreases in MRE occur over the coast and grassland surfaces where detection capabilities are poorest (Table 2), while over the ocean where (due to the nature of the algorithm) 2A12 detection capabilities are best, there is very little change in the MRE. Over all land surface types, the conditional (on both sensors detecting precipitation) CCs are very similar at ~0.6 and are slightly lower over the ocean and coast (Table 5).

The PDFs of occurrence (PDFc) and by precipitation volume (PDFv) are computed via the method proposed by Wolff and Fisher (2009) and provide a more detailed behavior of the two sensors' precipitation retrievals over each surface type (Figs. 9, 10). The PDFcs show the relative occurrence of a given sensor rain-rate estimate, while the PDFvs highlight the contribution of a particular rain-rate estimate to the total rain volume estimated by the sensor, which consequently lessens the impact of light rain rates and is therefore less reliant on the sensors' relative sensitivities (Kirstetter et al. 2013). Figure 9 shows that over the land and coast the distribution of 2A12's precipitation estimates relative to the reference is narrower and peaks at higher rain rates (at ~2–3 compared to $<1\,\mathrm{mm\,h^{-1}}$). This is likely due to the lower relative sensitivity and spatial resolution of both the TMI and the PR (from which the rain rate–Tb relationships are derived) relative to the reference, and also due to the general overestimation of convection by 2A12. Figure 10 reveals that, relative to the reference, 2A12 captures the precipitation volume distribution relatively well. However, a distinct bimodal structure is apparent in the TMI PDFvs, and while this structure can also be seen in the reference products, it is considerably less amplified and is scarcely visible over the woodland and cropland categories. The bimodal structure likely results from the greater volume contribution of higher rain rates and the greater occurrence of lower rain rates (specifically the $2–3\,\mathrm{mm\,h^{-1}}$ category of TMI). Over the ocean the 2A12 retrievals display considerably different

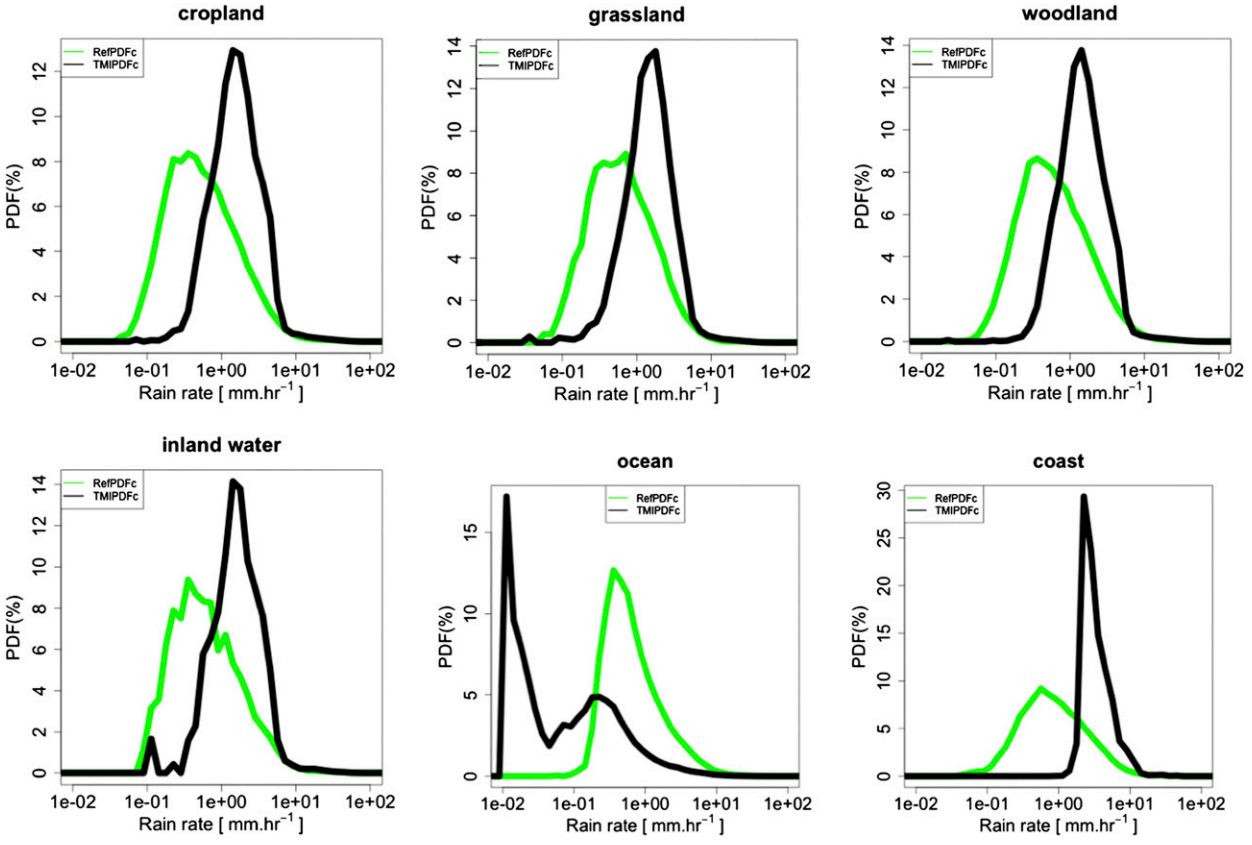

FIG. 9. PDFs of occurrence for the reference (green) and 2A12 (black) rainfall for the different surface types.

behavior, and a peak in the PDFc at very low rain rates is evident. This peak results from the probabilistic nature of the retrieval algorithm (Fig. 9), which results in many very low rain-rate estimates (which, if constrained by probability of precipitation values, would be set to zero). However, because of the greater robustness of the ocean algorithm, the general distribution of precipitation more closely matches the reference precipitation distribution, and only a slight general underestimation is apparent (Figs. 9, 10).

Figure 11 links the quality of 2A12's precipitation estimates with a number of precipitation characteristics, namely, intensity, classification, and spatial coverage. Figure 11a demonstrates that 2A12 has a tendency to overestimate light ($<5\,\mathrm{mm\,h^{-1}}$) precipitation while underestimating moderate to heavy precipitation, which is consistent with results from previous 2A12 studies (e.g., McCollum and Ferraro 2003; Wolff and Fisher 2009; Wang et al. 2009). 2A12's underestimation of high rain rates is primarily a result of the aforementioned factors that cause extreme precipitation rates to be smoothed, while the overestimation at low rain rates is likely a result of an overestimation of convective precipitation fraction (Fig. 11d). Over the land (where the precipitation quantification is highly dependent on precipitation classification), the tendency to overassign convection dominates and the overall MRE is positive. However, over the ocean where the effects of classification are not as significant, the smoothing effect dominates and the overall MRE is negative (Table 5).

The magnitude of the mean MRE is higher and the mean CC is lower over mixed precipitation events than purely stratiform or convective events; in particular, the CC is lowest and MRE highest (in magnitude) for primary stratiform events (CVF = 25%–50%; Figs. 11b,e). As discussed in section 3b, 2A12 tends to overassign convection in such events (Table 4), and this, along with the high gradients of precipitation generally present (within the TMI pixel) in these events, likely results in the large discrepancies between the two sensor's precipitation estimates. Meteorological examples of these events would include both decaying convection that still has a relatively active ice phase or MCSs. Midlatitude MCSs often contain both convective and stratiform components, and TMI pixels at the transition regions between the two precipitation regimes would likely contain large gradients of precipitation.

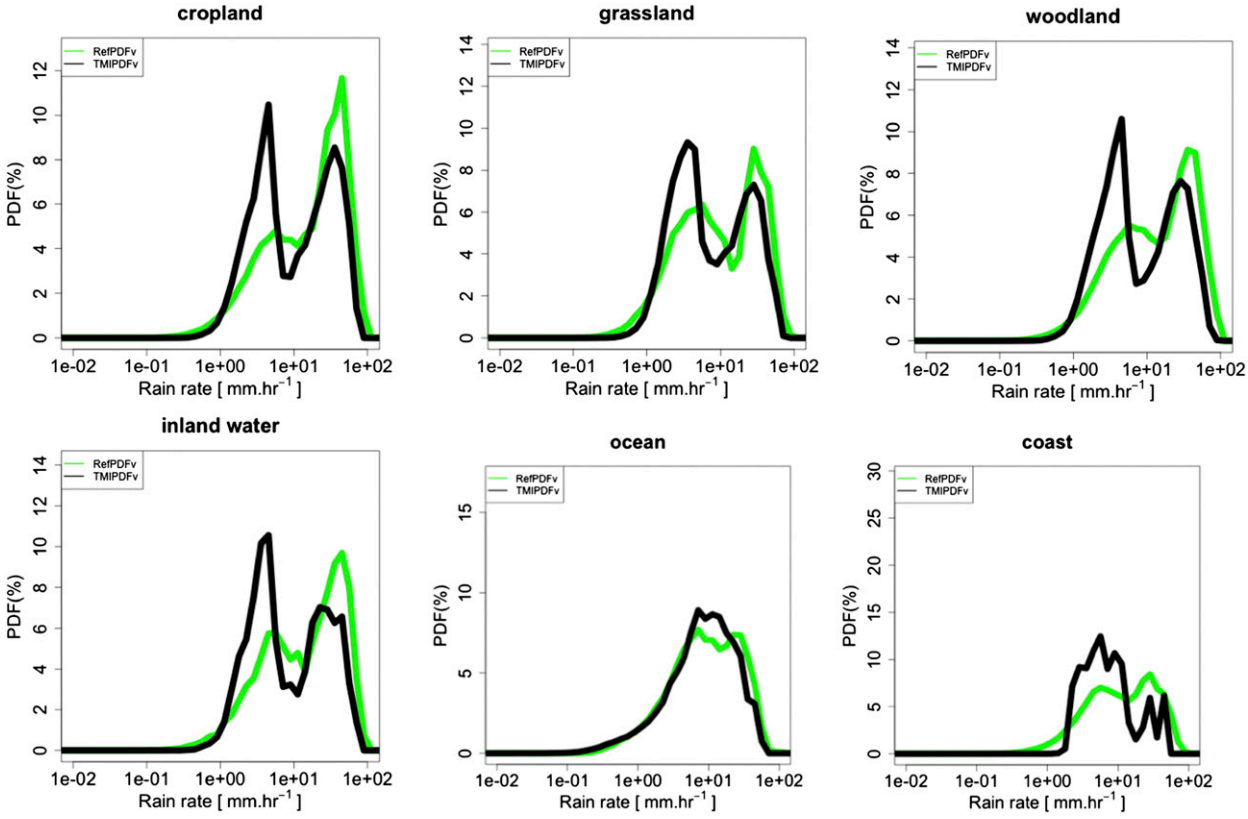

FIG. 10. PDFs of rainfall volume for the reference (green) and 2A12 (black) rainfall for the different surface types.

TMI 2A12's ability to quantify precipitation is also proportional to the spatial coverage of precipitation within the pixel, and a higher reference precipitation fraction is associated with both a lower MRE and a higher CC (Figs. 11c,f). This likely results from the high gradients of precipitation present in partially rain-filled pixels and is particularly magnified given the large size of the TMI pixel. While, it is very difficult to correct for this nonuniform beam filling (NUBF) effect at the algorithm-development level, it probably should be taken into account when utilizing TMI (and likely other PMW) precipitation estimates, as mean MREs greater than 1000% can be found in situations in which the pixel is <20% filled (Fig. 11c). Once again, it must be emphasized that the spatial coverage of precipitation and precipitation type (stratiform or convective) are not independent (Fig. 2a); consequently, it is difficult to disentangle their relative impacts on PMW retrievals.

4. Conclusions

To improve understanding of PMW error characteristics in anticipation of the GPM era of satellite QPE, TMI 2A12 rainfall products were compared at pixel level to high-resolution, high-quality reference ground radar–based rainfall products over the southern CONUS and nearshore ocean over a 7-month period (March–September 2011). The ability of version 7 of TMI's 2A12 to detect, classify, and quantify midlatitude precipitation was examined and linked to both surface and precipitation characteristics. Both precipitation and surface characteristics were found to significantly affect the accuracy of the TMI retrievals relative to the reference, and notable results are summarized below.

2A12 detects precipitation relatively well over all surface categories, except over the coast, when reference rain rates exceed 5 mm h^{-1} (Figs. 4a,d). However, 2A12 misses a significant portion of the precipitation spectrum below this threshold. Over the land, detection capabilities vary considerably with surface type and seem to degrade with decreasing soil moisture and vegetated fraction (Table 2, Fig. 4a). The low detection scores over the (generally) most arid surface (grassland) likely result from both the surface signal mimicking the scattering signal produced by ice-phase hydrometeors (resulting in false alarms) and the presence of isolated and shallow orographic precipitation, which is rarely detected by PMW sensors (resulting in missed events).

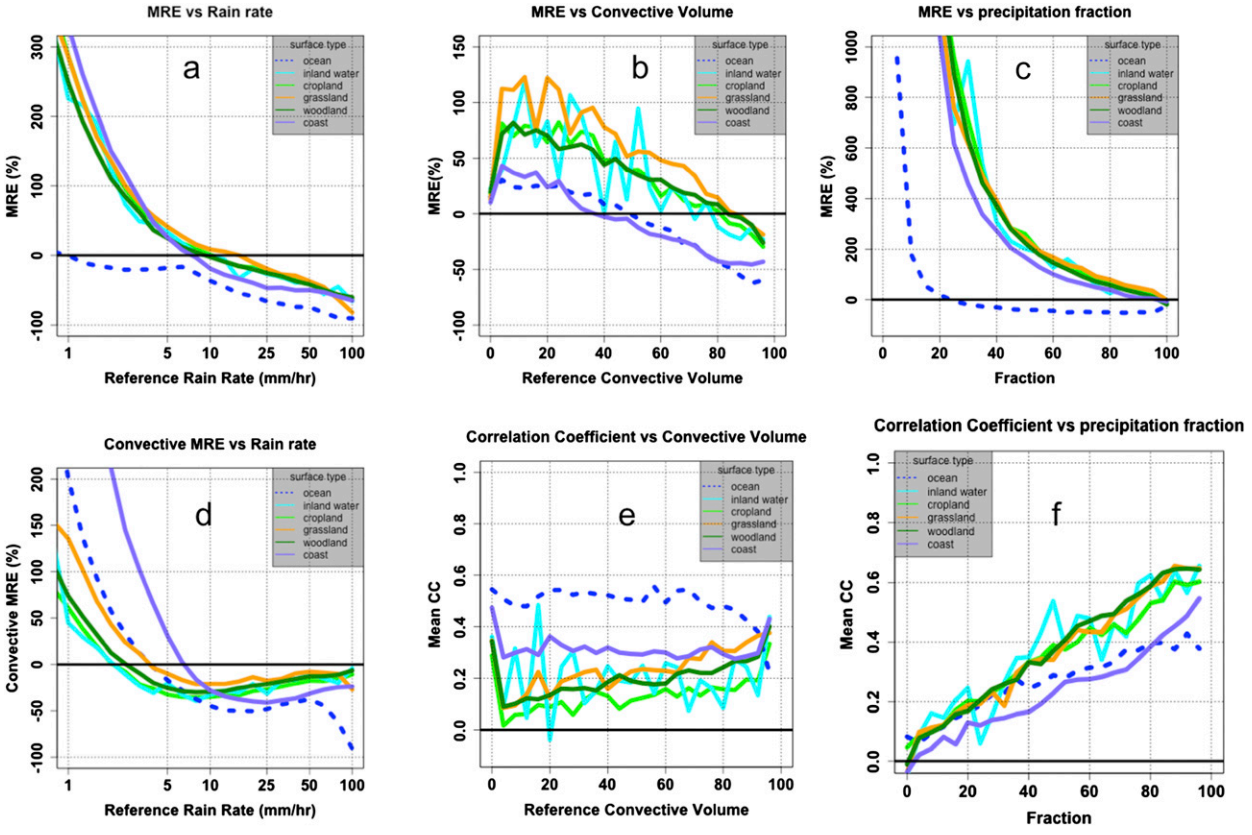

FIG. 11. MRE vs reference (a) rain rate, (b) CVF, and (c) PF. (d) Convective MRE vs reference rain rate. (e) Mean CC vs reference CVF. (f) Mean CC vs reference PF.

Over the coastal regions, the large gradient of emissivity within the footprint necessitates a fairly conservative retrieval algorithm and thus results in a very low probability of detection. 2A12's detection capabilities are also dependent on the characteristics of the precipitation within the footprint (Figs. 4b,c) and specifically are proportional to the spatial coverage of the precipitation within the footprint; isolated or small-scale precipitation features are detected at a fairly low rate. Precipitation detection improves with increasing convective occurrence of precipitation, likely due to its generally more prominent ice phase and more extensive spatial coverage. It was not possible in the current study to evaluate the detection capabilities over the ocean, as the ocean algorithm does not apply a simple rain/no-rain mask as is done over the coast and land and instead utilizes a probabilistic approach.

Regarding precipitation classification, 2A12 is able to detect and quantify convection relatively well, particularly as the proportion of convective precipitation increases within the footprint (Fig. 5a). However, 2A12 tends to overestimate convection significantly over the grassland, coastal, and ocean categories (Table 4, Fig. 6). Over grassland, this likely results from the (arid) surface signal mimicking convection, and over the ocean and coastal regions this results from the Bayesian retrieval algorithm. The majority of misclassification by 2A12 over the land tends to occur in mixed stratiform–convective precipitation events. Specifically, 2A12 underrepresents the number of primarily stratiform events while overestimating the number of primarily convective events. Over the land, the classification accuracy of 2A12 relative to the reference was shown to be the primary factor influencing the accuracy of rain-rate estimates (Fig. 8).

Regarding precipitation quantification, when precipitation detection is ignored, 2A12 exhibits positive relative errors over all surfaces except the ocean and specifically tends to underestimate high rain rates while overestimating low rain rates (Table 5; Figs. 10, 11a). The overestimation at low rain rates is most apparent over the land and appears to be primarily driven by 2A12's overestimation of convective fraction (Figs. 8, 11d) and consequently is magnified over sparsely vegetated surfaces. Over the ocean, TMI 2A12 generally underestimates precipitation relative to the reference

despite overestimating the convective fraction (Tables 4, 5). This underestimation is likely a result of the Bayesian framework employed by the retrieval algorithm(s), the comparatively large size of the TMI footprint, and sensor saturation at high rain rates, all of which limit the ability of 2A12 to capture extreme rain rates. These smoothing effects are also seen over the other surfaces at high rain rates, yet the overall MRE is still positive because of the overestimation of convection. When detection is considered, the MRE decreases dramatically over most surface types, as the effects of overassigning convection are at least partially offset by the significant amount of rainfall missed by the (less sensitive) TMI (Table 5).

Precipitation quantification was also linked to precipitation characteristics, specifically precipitation classification and spatial coverage. Over the land, a lower MRE and higher CC are associated with purely stratiform and purely convective events, while the errors increase in mixed stratiform–convective events (Figs. 11b,e). This decrease in retrieval quality possibly results from both the high gradients of precipitation present in mixed events and a dearth of mixed cases in the retrieval database. A lower MRE and higher CC are also associated with greater filling of the TMI pixel, and precipitation estimates in pixels under 50% filled showed very high relative errors, a probable result of the high gradients of precipitation within the pixel (Figs. 11c,f).

Future work will involve applying a similar methodology (although adjusted somewhat to compensate for the shift to Bayesian retrievals over the land) to evaluate PMW sensors associated with the GPM (both constellation radiometers and the GMI), focusing on their performance in common midlatitude precipitation regimes such as mixed stratiform–convective, orographic, and frontal precipitation events. It would also be particularly beneficial to examine the impacts of the newly operational surface properties database (which are used to constrain the retrievals) on GPM-era PMW precipitation retrievals. As these surface classifications are more closely linked to surface microwave radiometric characteristics than the MODIS land surface classifications, the effects of the surface properties on retrievals may be more pronounced. The greater latitude range covered by the GPM-related sensors would also greatly increase the number of inland water body samples, allowing a much more robust analysis of PMW retrievals over inland water bodies. Future work will also involve evaluating the propagation of errors from the instantaneous precipitation estimates (level 2 products) to the level 3 gridded average precipitation products. A longer-term goal would be to incorporate knowledge of PMW error characteristics (obtained through studies similar to this one) into GPM-era probabilistic precipitation retrievals. This would greatly facilitate the assimilation of these retrievals into ensemble-based hydrometeorological models.

Acknowledgments. We are very much indebted to the team responsible for the Q2 products, especially Carrie Langston. We thank Dr. G. Huffman for very insightful comments. The lead author was supported by a grant from the NASA Global Precipitation Measurement Mission Ground Validation Management. The work was cosupported by a NASA Precipitation Measurement Mission grant.

REFERENCES

Aires, F., C. Prigent, F. Bernardo, C. Jiménez, R. Saunders, and P. Brunel, 2011: A tool to estimate land-surface emissivities at microwave frequencies (TELSEM) for use in numerical weather prediction. *Quart. J. Roy. Meteor. Soc.,* **137,** 690–699, doi:10.1002/qj.803.

Bakker, M. H. N., 2009: Transboundary river floods and institutional capacity. *J. Amer. Water Resour. Assoc.,* **45,** 553–566, doi:10.1111/j.1752-1688.2009.00325.x.

Bauer, P., J.-F. Mahfouf, W. S. Olson, F. S. Marzano, S. D. Michele, A. Tassa, and A. Mugnai, 2002: Error analysis of TMI rainfall estimates over ocean for variational data assimilation. *Quart. J. Roy. Meteor. Soc.,* **128,** 2129–2144, doi:10.1256/003590002320603575.

Brier, G. W., and R. A. Allen, 1952: Verification of weather forecasts. *Compendium of Meteorology,* T. F. Malone, Ed., Amer. Meteor. Soc., 841–848.

Ferraro, R., and Coauthors, 2013: An evaluation of microwave land surface emissivities over the continental United States to benefit GPM-era precipitation algorithms. *IEEE Trans. Geosci. Remote Sens.,* **51,** 378–398, doi:10.1109/TGRS.2012.2199121.

Friedl, M. A., D. Sulla-Menashe, B. Tan, A. Schneider, N. Ramankutty, A. Sibley, and X. Huang, 2010: MODIS Collection 5 global land cover: Algorithm refinements and characterization of new datasets, 2001–2012. *Remote Sens. Environ.,* **114,** 168–182, doi:10.1016/j.rse.2009.08.016.

Gopalan, K., N. Y. Wang, R. Ferraro, and C. Liu, 2010: Status of the TRMM 2A12 land precipitation algorithm. *J. Atmos. Oceanic Technol.,* **27,** 1343–1354, doi:10.1175/2010JTECHA1454.1.

Grecu, M., and E. Anagnostou, 2001: Overland precipitation estimation from TRMM passive microwave observations. *J. Appl. Meteor.,* **40,** 1367–1380, doi:10.1175/1520-0450(2001)040<1367:OPEFTP>2.0.CO;2.

Hou, A. Y., S. Q. Zhang, A. M. da Silva, W. S. Olson, C. D. Kummerow, and J. Simpson, 2001: Improving global analysis and short-range forecast using rainfall and moisture observations derived from TRMM and SSM/I passive microwave sensors. *Bull. Amer. Meteor. Soc.,* **82,** 659–680, doi:10.1175/1520-0477(2001)082<0659:IGAASF>2.3.CO;2.

Kirstetter, P. E., and Coauthors, 2012: Toward a framework for systematic error modeling of NASA spaceborne radar with NOAA/NSSL ground radar–based National Mosaic QPE. *J. Hydrometeor.,* **13,** 1285–1300, doi:10.1175/JHM-D-11-0139.1.

——, N. Viltard, and M. Gosset, 2013: An error model for instantaneous satellite rainfall estimates: Evaluation of BRAIN-TMI over West Africa. *Quart. J. Roy. Meteor. Soc.,* **139,** 894–911, doi:10.1002/qj.1964.

——, Y. Hong, J. J. Gourley, Q. Cao, M. Schwaller, and W. Petersen, 2014: Research framework to bridge from the Global Precipitation Measurement mission core satellite to the constellation sensors using ground-radar-based National Mosaic QPE. *Remote Sensing of the Terrestrial Water Cycle, Geophys. Monogr.,* Vol. 206, Amer. Geophys. Union, 61–80, doi:10.1002/9781118872086.ch4.

——, ——, ——, M. Schwaller, W. Petersen, and Q. Cao, 2015: Impact of sub-pixel rainfall variability on spaceborne precipitation estimation: Evaluating the TRMM 2A25 product. *Quart. J. Roy. Meteor. Soc.,* **141,** 953–966, doi:10.1002/qj.2416.

Kitzmiller, K., and Coauthors, 2011: Evolving multisensor precipitation estimation methods: Their impacts on flow prediction using a distributed hydrologic model. *J. Hydrometeor.,* **12,** 1414–1431, doi:10.1175/JHM-D-10-05038.1.

Kummerow, C., W. Barnes, T. Kozu, J. Shiue, and J. Simpson, 1998: The Tropical Rainfall Measuring Mission (TRMM) sensor package. *J. Atmos. Oceanic Technol.,* **15,** 809–817, doi:10.1175/1520-0426(1998)015<0809:TTRMMT>2.0.CO;2.

——, and Coauthors, 2001: The evolution of the Goddard profiling algorithm (GPROF) for rainfall estimation from passive microwave sensors. *J. Appl. Meteor.,* **40,** 1801–1820, doi:10.1175/1520-0450(2001)040<1801:TEOTGP>2.0.CO;2.

——, S. Ringerud, J. Crook, D. Randel, and W. Berg, 2011: An observationally generated a priori database for microwave rainfall retrievals. *J. Atmos. Oceanic Technol.,* **28,** 113–130, doi:10.1175/2010JTECHA1468.1.

Lakshmanan, V., A. Fritz, T. Smith, K. Hondl, and G. Stumpf, 2007: An automated technique to quality control radar reflectivity data. *J. Appl. Meteor. Climatol.,* **46,** 288–305, doi:10.1175/JAM2460.1.

Lin, X., and A. Y. Hou, 2008: Evaluation of coincident passive microwave rainfall estimates using TRMM PR and ground measurements as references. *J. Appl. Meteor. Climatol.,* **47,** 3170–3187, doi:10.1175/2008JAMC1893.1.

Liu, C., and E. J. Zipser, 2009: "Warm rain" in the tropics: Seasonal and regional distribution based on 9 years of TRMM data. *J. Climate,* **22,** 767–779, doi:10.1175/2008JCLI2641.1.

McCollum, J., and R. Ferraro, 2003: Next generation of NOAA/NESDIS TMI, SSM/I, and AMSR-E microwave land rainfall algorithms. *J. Geophys. Res.,* **108,** 8382, doi:10.1029/2001JD001512.

——, and ——, 2005: Microwave rainfall estimation over coasts. *J. Atmos. Oceanic Technol.,* **22,** 497–512, doi:10.1175/JTECH1732.1.

Moisseev, D., E. Saltikoff, and M. Leskinen, 2009: Using dual-polarization weather radar observations to improve quantitative precipitation estimation in snowfall. *Proceedings of the 8th International Symposium on Troposheric Profiling,* A. Apituley, H. W. J. Russchenberg, and W. A. A. Monna, Eds., Royal Netherlands Meteorological Institute, S11-O04.

Olson, W. S., Y. Hong, C. D. Kummerow, and J. Turk, 2001: A texture polarization method for estimating convective–stratiform precipitation area coverage from passive microwave radiometer data. *J. Appl. Meteor.,* **40,** 1577–1591, doi:10.1175/1520-0450(2001)040<1577:ATPMFE>2.0.CO;2.

Petty, G. W., 1994: Physical Retrievals of over-ocean rain rate from multichannel microwave imagery. Part II: Algorithm Implementation. *Meteor. Atmos. Phys.,* **54,** 101–124, doi:10.1007/BF01030054.

Prabhakara, C., R. Icovazzi Jr., J. A. Weinman, and G. Dalu, 2000: A TRMM microwave radiometer rain rate estimation method with convective and stratiform discrimination. *J. Meteor. Soc. Japan,* **78,** 241–258.

Shige, S., S. Kida, H. Ashiwake, T. Kubota, and K. Aonashi, 2013: Improvement of TMI rain retrievals in mountainous areas. *J. Appl. Meteor. Climatol.,* **52,** 242–254, doi:10.1175/JAMC-D-12-074.1.

Steiner, M., R. A. Houze, and S. E. Yuter, 1995: Climatological characterization of three-dimensional storm structure from operational radar and rain gauge data. *J. Appl. Meteor.,* **34,** 1978–2007, doi:10.1175/1520-0450(1995)034<1978:CCOTDS>2.0.CO;2.

Stephens, G. L., and C. D. Kummerow, 2007: The remote sensing of clouds and precipitation from space: A review. *J. Atmos. Sci.,* **64,** 3742–3765, doi:10.1175/2006JAS2375.1.

Tian, Y., and C. D. Peters-Lidard, 2007: Systematic anomalies over inland water bodies in satellite-based precipitation estimates. *Geophys. Res. Lett.,* **34,** L14403, doi:10.1029/2007GL030787.

Varma, A. K., G. Liu, and Y.-J. Noh, 2004: Subpixel-scale variability of rainfall and its application to mitigate the beam-filling problem. *J. Geophys. Res.,* **109,** D18210, doi:10.1029/2004JD004968.

Vasiloff, S., and Coauthors, 2007: Improving QPE and very short term QPF: An initiative for a community-wide integrated approach. *Bull. Amer. Meteor. Soc.,* **88,** 1899–1911, doi:10.1175/BAMS-88-12-1899.

Wang, N. Y., C. Liu, R. Ferraro, D. Wolff, E. Zipser, and C. Kummerow, 2009: The TRMM 2A12 land precipitation product—Status and future plans. *J. Meteor. Soc. Japan,* **87A,** 237–253, doi:10.2151/jmsj.87A.237.

Weng, F., T. Zhu, and B. Yan, 2007: Satellite data assimilation in numerical weather prediction models. Part II: Uses of rain-affected radiances from microwave observations for hurricane vortex analysis. *J. Atmos. Sci.,* **64,** 3910–3925, doi:10.1175/2006JAS2051.1.

Wilheit, T., C. D. Kummerow, and R. Ferraro, 2003: Rainfall algorithms for AMSR-E. *IEEE Trans. Geosci. Remote Sens.,* **41,** 204–214, doi:10.1109/TGRS.2002.808312.

Wilks, D. S., 2011: *Statistical Methods in the Atmospheric Sciences.* Elsevier, 676 pp.

Wolff, D. B., and B. L. Fisher, 2008: Comparisons of instantaneous TRMM ground validation and satellite rain-rate estimates at different spatial scales. *J. Appl. Meteor. Climatol.,* **47,** 2215–2237, doi:10.1175/2008JAMC1875.1.

——, and ——, 2009: Assessing the relative performance of microwave-based satellite rain-rate retrievals using TRMM ground validation data. *J. Appl. Meteor. Climatol.,* **48,** 1069–1099, doi:10.1175/2008JAMC2127.1.

Zhang, J., K. Howard, and J. J. Gourley, 2005: Constructing three-dimensional multiple radar reflectivity mosaics: Examples of convective storms and stratiform rain echoes. *J. Atmos. Oceanic Technol.,* **22,** 30–42, doi:10.1175/JTECH-1689.1.

——, and Coauthors, 2011a: National Mosaic and Multi-Sensor QPE (NMQ) system: Description, results and future plans. *Bull. Amer. Meteor. Soc.,* **92,** 1321–1338, doi:10.1175/2011BAMS-D-11-00047.1.

——, Y. Qi, K. Howard, C. Langston, and B. Kaney, 2011b: Radar Quality Index (RQI)—A combined measure of beam blockage and VPR effects in a national network. *IAHS Publ.,* **351,** 388–393.